CHEMISTRY OF MATERIALS

h-MBenes (M/B = 1:1) as Promising Electrocatalysts for Nitrogen Reduction Reaction: A Theoretical Study

Shuang Feng, Yufang Yao, Jean-Christophe Charlier, Gian-Marco Rignanese, and Junjie Wang*

Cite This: *Chem. Mater.* 2023, 35, 9019−9028

Read Online

ACCESS | Metrics & More | Article Recommendations | Supporting Information

ABSTRACT: MAB phases and their two-dimensional (2D) derivatives MBenes have attracted increasing attention in electrochemical catalysis because of their unique structures and inherent electronic properties. Since the first hexagonal MAB (*h*-MAB) phase Ti_2InB_2 and 2D TiB *h*-MBene were discovered in 2019, the family of *h*-MBenes shows a promising perspective in electrochemical applications. In this work, the electrochemical nitrogen reduction reaction (eNRR) properties of discovered *h*-MBenes are studied theoretically for the first time. A volcano-shaped relationship between the limiting potential (U_L) and the adsorption energy of the **NNH group (ΔE_{NNH}) is established. Moreover, it is found that the catalytic activity can be engineered by the bimetallic alloying effect, which applies to both in-plane ordered *h*-$M'_{2/3}M''_{1/3}B$ phases and *h*-MBs with a second transition metal alloyed. Remarkably, guided by the revealed volcano-shaped relationship, Rh-alloyed hexagonal 2D WB and NbB with U_L as small as −0.34 and −0.56 V, respectively, are designed. Finally, the transition metal alloying is revealed to regulate the orbital energy redistribution, consequently adjusting the binding strength of N-containing intermediates with *h*-MBene surfaces to an appropriate range. This work unravels the promise of *h*-MBenes as eNRR catalysts and can shed light on the potential for *h*-MBenes in extensive electrochemical applications.

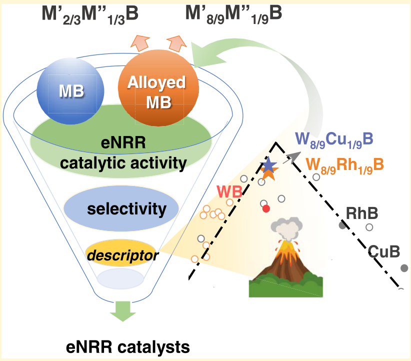

1. INTRODUCTION

Ammonia (NH_3) is an essential feedstock for the preparation of fertilizers, explosives, pharmaceuticals, etc., and is also a sustainable carbon-free energy source for achieving zero-carbon emissions.[1] However, because the industrial NH_3 production method, the Haber−Bosch process requires large amounts of energy[2] to maintain harsh conditions[3] (400−500 °C and 150−250 atm), and it generates more than 450 million tons of greenhouse gases per year, accounting for 1% of global emissions.[4] Therefore, with the increasingly serious energy crisis and the environmental problems linked to the present NH_3 production, the exploration of cleaner, energy-saving, and efficient ammonia synthesis methods has become a major topic of research.[5]

The strong N≡N triple bond is the main reason why the thermal catalysis of ammonia synthesis needs to be carried out under the conditions of high temperature and high pressure. It has been reported that the N≡N triple bond is weakened and completely decomposed during electrochemical hydrogenation until the first NH_3 is released.[6,7] Notably, water can act as a proton source in an aqueous environment to facilitate the recyclability and efficiency of nitrogen reduction reaction (eNRR).[8] Therefore, eNRR occurs under milder conditions with less energy injected at the start of the reaction and provides a promising solution for green ammonia synthesis.[9] In particular, with the rapid development of solar or wind power generation, eNRR supported by green electricity holds a very attractive prospect.

The central problem to be solved in eNNR research is the development of high-performance catalytic materials. Transition metals (TMs) are by far the most popular catalysts for N_2 activation and protonation[10,11] because they can activate N_2 through a "π-backdonation" mechanism[12] and interact with reaction intermediates, ultimately facilitating a smooth reaction process.[13] In particular, noble metals, such as Ru, have been extensively studied as eNRR catalysts.[14] However, the scarcity and low atomic utilization make the use of noble metals uneconomical. Moreover, the catalytic activity and selectivity of available eNRR electrocatalysts, even for noble metals, are still low.[15−18] This results in two major problems of eNRR, namely, low yield and low Faradaic efficiency, which seriously hinder further research and the use of eNRR. Consequently, developing efficient electrocatalysts remains the greatest challenge in eNRR research.[19,20]

Two-dimensional (2D) materials have received a lot of attention[21,22] since the remarkable properties of graphene were discovered.[23] Quite interestingly, 2D transition metal compounds (TMCs) inherit the superior catalytic activity of TMs

Received: July 3, 2023
Revised: October 6, 2023
Accepted: October 9, 2023
Published: October 20, 2023

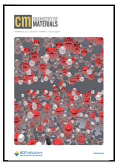

https://doi.org/10.1021/acs.chemmater.3c01656

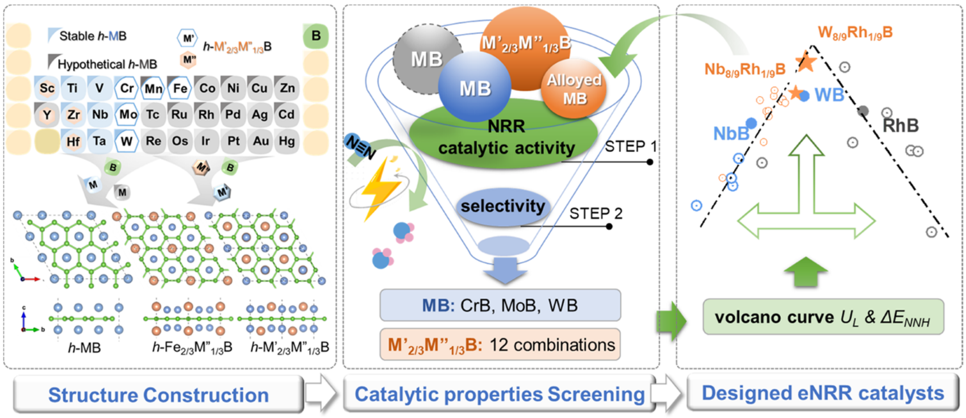

Figure 1. Schematic diagram of the workflow, including the structure construction, the screening based on the eNRR catalytic properties, and the design of eNRR binary 2D *h*-MBs and ternary 2D *h*-$M'_{2/3}M''_{1/3}B$ catalysts. For *h*-$M'_{2/3}M''_{1/3}B$, the two possible structures are shown on the right of the left panel: the left one in which the metal layers are mirrored with respect to the B layer is that of *h*-$Fe_{2/3}M''_{1/3}B$, while the right one is for all other *h*-$M'_{2/3}M''_{1/3}Bs$ (M′ is Cr, Mn, Mo, and W).

and present well-defined active sites, which constitute important advantages in the field of electrochemistry.[24,25] In particular, non-vdW 2D TMCs, such as MXenes[26−29] and more specifically MBenes,[30−33] are known to be rich in coordinatively unsaturated active sites, which are beneficial for charge and mass transfer during catalysis. For example, it has been demonstrated that MoC_2,[34] Mo_2B_2, and Fe_2B_2[35] exhibit outstanding electrochemical properties. Additionally, MBenes serve as an ideal matrix for supporting signal-atom catalysts.[36,37] However, research on MBenes in the field of electrochemistry is still in its early stages[38,39] and has primarily focused on orthorhombic MAB.[40,41] Moreover, although theoretical calculations show that MBenes have a great potential in electrochemical catalysis,[42] how to obtain MBenes from their parent material MAB phases remains a great challenge.[43]

Since 2019, various new hexagonal MAB (*h*-MAB) phases (M_2AB_2, M_2AB, and M_3AB_4),[44,45] which differ from the traditional orthorhombic MAB (*o*-MAB) phases,[46] have been predicted through evolutionary structure search. One such structure Ti_2InB_2 was successfully synthesized and the indium layers can be removed experimentally to form layered TiB.[44] Notably, *h*-MBs, the derivatives of *h*-M_2AB_2, have diverse stable phases, including ScB, TiB, VB, CrB, MnB, ZrB, NbB, MoB, HfB, TaB, and WB according to theoretical calculations.[47,48] These bare *h*-MBs show great advantages on N_2 adsorption and reduction. Furthermore, just as in in-plane ordered MAX (*i*-MAX) phases,[49] a second element can be introduced in *h*-M_2AB_2 to form the *h*- $(M'_{2/3}M''_{1/3})_2AB_2$ alloy. This has been verified theoretically[50−52] and experimentally.[53] This is quite different from the bimetallic *o*-MAB, which can only form a solid solution.[50,54] Therefore, *h*-MABs are more advantageous in the study of catalytic performance than *o*-MABs. Moreover, theoretical[55] and experimental[56,57] studies have demonstrated the promising exfoliation feasibility in the M/B = 1:1 family (*h*-M_2AB_2 and *h*-$(M'_{2/3}M''_{1/3})_2AB_2$). In 2020, Rosen and co-workers successfully synthesized two-dimensional $Mo_{4/3}B_{2-x}$ and reported their excellent HER catalytic activity.[50] Therefore, *h*-MBenes with M/B = 1:1 can provide a wide variety of samples for screening for excellent eNRR catalysts, and in-plane ordered *h*-$M'_{2/3}M''_{1/3}B$ have unparalleled advantages. Therefore, it is of great significance to explore the eNRR catalytic properties of *h*-MBenes and the effect of alloying on the electrochemical properties of bimetallic *h*-MBenes.

In this work, a systematic theoretical study of the eNRR catalytic activity and selectivity of 2D *h*-MBs and *h*-$M'_{2/3}M''_{1/3}Bs$ is performed as illustrated in Figure 1. The choice strategy of transition metals is illustrated in the left panel of Figure 1. First, it is demonstrated that 2D CrB, MoB, and WB can be promising eNRR electrocatalysts based on calculations of the Gibbs free energy (as illustrated in the central panel of Figure 1). Then, a volcano-shaped relationship between the eNRR limiting potential (U_L) and the adsorption energy of the **NNH intermediate (ΔE_{NNH}) is established by combining theoretical results performed on both real and hypothetical 2D *h*-MB structures (as shown in the right panel of Figure 1). This relationship is used to design bimetallic *h*-$M'_{2/3}M''_{1/3}B$ catalysts, hence demonstrating good transferability of the ΔE_{NNH} descriptor for eNRR in *h*-MBene systems. Furthermore, an investigation of the alloying effect in *h*-$M'_{2/3}M''_{1/3}B$ shows that the eNRR catalytic activity is mainly attributed to the electron distribution of the d_{z^2} orbitals of the M′ and M″ transition metals. Moreover, inspired by the revealed alloying effect, it is further confirmed that the combination of two 2D *h*-MB phases located on the two branches of the volcano curve can lead to a compound, which inherits the advantages of both and achieves an excellent activity close to the volcano peak by alloying with a second TM. For instance, the limiting potentials of 2D NbB and WB can be shifted from −0.74 to −0.54 V and from −0.56 to −0.34 V, respectively, by alloying with Rh atoms.

2. METHODS

All calculations were performed using the spin-polarized density functional theory (DFT) method based on the projector augmented wave (PAW) approach,[58] as implemented in the Vienna Ab inito Simulation Package (VASP).[59,60] The exchange−correlation energy was modeled using the Perdew−Burke−Ernzerhof (PBE) functional within the generalized gradient approximation (GGA)[61] framework. This choice was made based on the proven accuracy of the PBE functional in calculating Gibbs free energy.[37] An energy cutoff of 550 eV was used for the plane-wave basis set. The van der Waals interactions were also taken into account by including a semiempirical correction scheme developed by Grimme et al. (DFT-D3).[62] The convergence criteria for the energy and the forces were set to 10^{-5} and 0.02 eV/Å, respectively. The Brillouin zone was sampled by adopting

https://doi.org/10.1021/acs.chemmater.3c01656
Chem. Mater. 2023, 35, 9019−9028

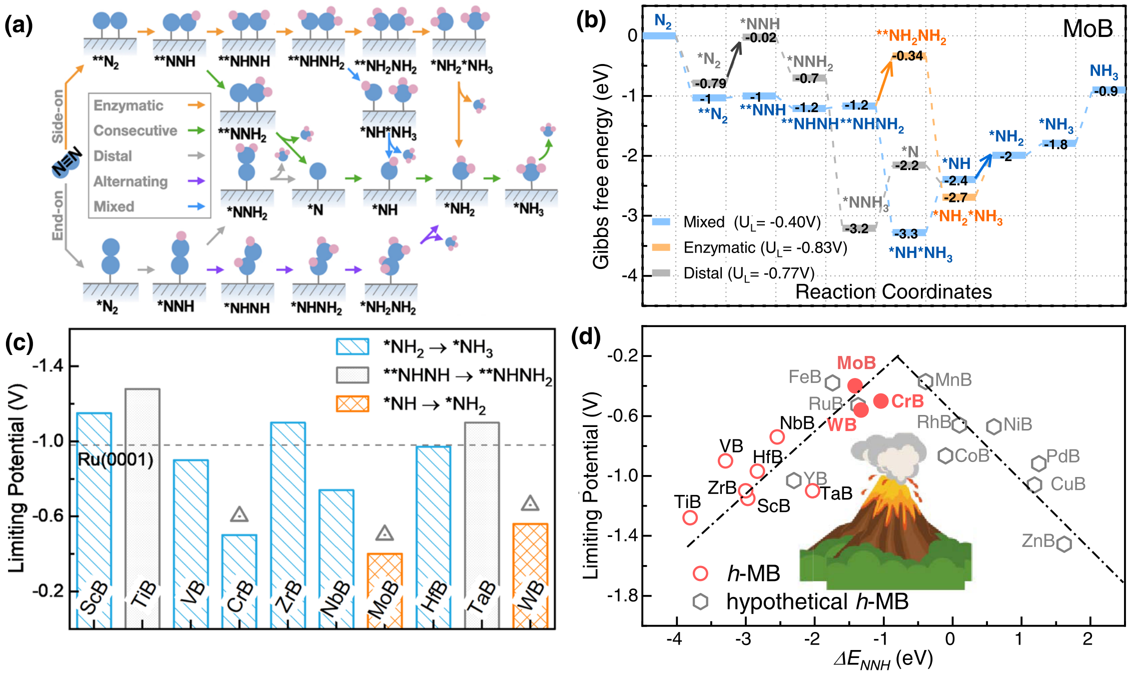

Figure 2. Catalytic properties of 2D *h*-MBs. (a) Schematic diagram of the associative mechanism for NH_3 electrochemical production; (b) calculated reaction pathways for 2D MoB starting from the side-on and end-on adsorption configurations of N_2; (c) calculated limiting potential (U_L vs SHE) for the stable *h*-MBs with the corresponding PDS ($^*NH_2 \rightarrow {}^*NH_3$ in blue, $^{**}NHNH \rightarrow {}^{**}NHNH_2$ in gray, and $^*NH \rightarrow {}^*NH_2$ in orange); and (d) volcano-shaped relationship between U_L and the **NNH adsorption energy (ΔE_{NNH}). The dashed line in panel (c) indicates the reported limiting potential of the Ru(0001) surface as a reference for the eNRR catalytic activity and triangles above CrB, MoB, and WB indicate that these U_L are lower than −0.6 V. The red circles and gray hexagons in panel (d) represent the stable and hypothetical *h*-MBs, respectively.

5 × 5 × 1 and 11 × 11 × 1 Monkhorst−Pack *k*-points meshes for the structural optimizations and for the electronic calculations, respectively. The choice of the cutoff energy and *k*-point sampling was verified by performing convergence tests (Tables S1 and S2). Slab models were constructed to simulate the 2D structures of *h*-MBenes, introducing 20 Å of vacuum space to avoid spurious interaction between the periodic units along the vertical direction. 3 × 3 × 1 and 2 × 2 × 1 supercells were built for 2D *h*-MB and $h\text{-}M'_{2/3}M''_{1/3}B$ structures, respectively, to ensure the same number of surface atoms as well as similar lattice parameters in all 2D models. Crystal orbital Hamilton population (COHP)[63,64] calculations were performed using the LOBSTER code to analyze the chemical bonding of *h*-MBenes. The VASPKIT[65] package was used for data postprocessing. The VESTA code was employed for the visualization of the structural configurations and the differential charge density analysis.[66]

In the framework of the electrochemical reduction process, the Gibbs free energy plays a critical role in evaluating the performance of catalysts. Therefore, the Gibbs free energy change was calculated for each step using the following formula

$$\Delta G_{\text{ads}} = \Delta E_{\text{ads}} + \Delta \text{ZPE} - T\Delta S \tag{1}$$

where ΔE_{ads} is the energy change of each hydrogenation reaction, ΔZPE is the zero-point energy correction of each reaction, T is the operating temperature set as 300 K, and ΔS is the entropy correction of each reaction.

Because the NRR reaction is a six-step hydrogenation reaction that can be expressed by

$$^*\text{R} + \text{H}^+ + \text{e}^- \rightarrow {}^*\text{RH} \tag{2}$$

where *R and *RH represent the N-containing intermediates and ΔG represents Gibbs energy change of hydrogenations. The corresponding enthalpy change can be calculated as

$$\Delta G = \Delta G_{\text{RH}} - \Delta G_{\text{R}} - \Delta G_{(\text{H}^+ + \text{e}^-)} \tag{3}$$

The transfers of protons and electrons were described using the computational hydrogen electrode (CHE) model proposed by Nørskov and co-workers,[67] where the electrode potential related to the standard hydrogen electrode (*U* vs SHE) can be expressed as

$$\mu(\text{H}^+) + \mu(\text{e}^-) \rightarrow \frac{1}{2}\mu(\text{H}_2) - eU \tag{4}$$

The Gibbs free energy of the proton−electron pair was obtained for standard conditions as

$$\text{H}^+(\text{aq}) + \text{e}^- = \frac{1}{2}\text{H}_2\ (\text{g});\ \Delta G^\circ = 0\ \text{eV} \tag{5}$$

That is, the total free energy of the proton−electron pair (H^+ (aq) + e^-) is equal to half that of H_2 (g). The energy of H_2 (g) as well as other intermediates was calculated at a temperature of 300 K and a pressure of 1 atm.

The potential-determining step (PDS) is the one with the largest calculated Gibbs free energy change (ΔG), and the limiting potential (U_L) is the corresponding electrode potential, which is expressed as follows

$$U_{\text{L}} = \frac{\Delta G}{e} \tag{6}$$

3. RESULTS AND DISCUSSION

Herein, the eNRR catalytic properties of binary 2D *h*-MB phases (M is Sc, Ti, V, Cr, Zr, Nb, Mo, Hf, Ta, and W) were systematically studied. First, the magnetic moments of 2D *h*-MBs were studied. It was found that, among 10 stable *h*-MBs, only CrB is antiferromagnetic, while the other 9 are nonferromagnetic. Previous studies have confirmed that the electrochemical reduction of N_2 will occur along the associative mechanism[68] as shown in Figure 2a. It shows that starting from lateral (side-on) and vertical (end-on) adsorption configurations of N_2, there are four traditional reaction pathways, namely, enzymatic, consecutive, distal, and alternat-

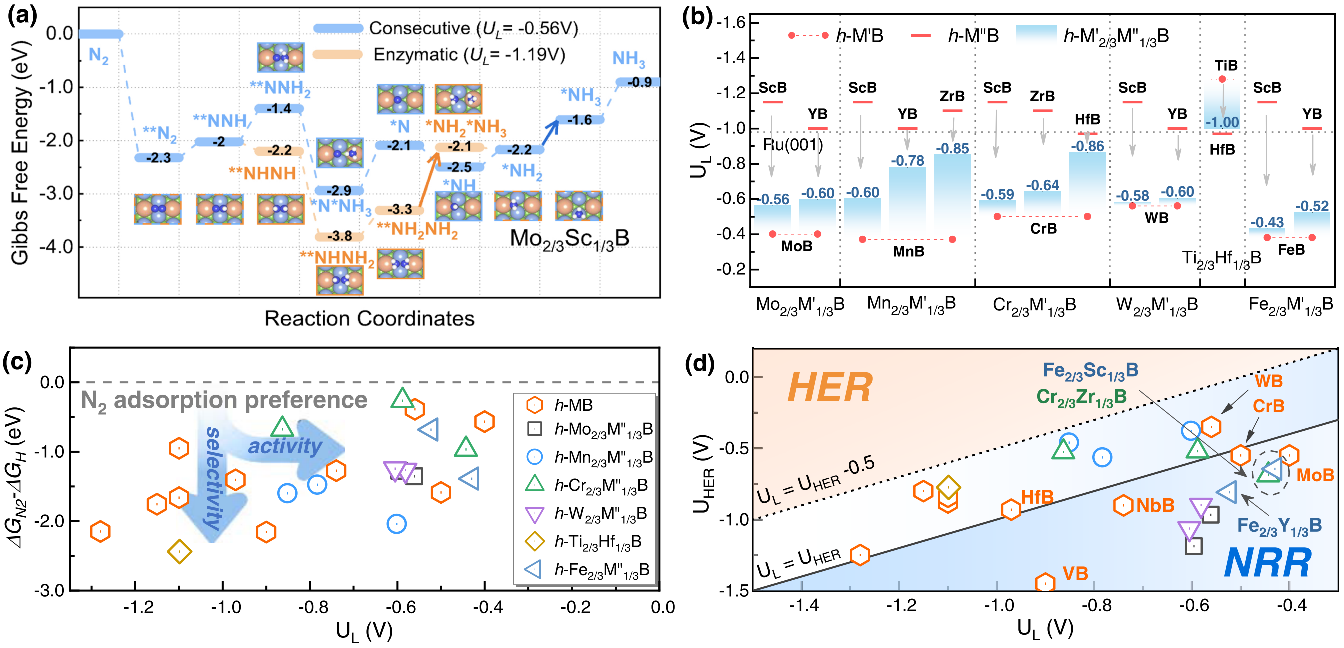

Figure 3. Effect of alloying on the catalytic properties of 2D hexagonal borides. (a) Schematic diagram of the reaction pathways and Gibbs free energy for N_2 hydrogenation on 2D $Mo_{2/3}Sc_{1/3}B$ (the calculations are based on the side-on configuration for N_2 adsorption); (b) calculated U_L of bimetallic h-$M'_{2/3}M''_{1/3}B$ in comparison with those of corresponding h-M′B and h-M″B phases; (c) difference between the calculated adsorption energy of $^{**}N_2$ and *H ($\Delta G_{N_2} - \Delta G_H$) on h-MBs and h-$M'_{2/3}M''_{1/3}$Bs as a function limiting potential U_L. (d) Relationship between the limiting potentials of HER (U_{HER}) and eNRR (U_L). The pictures in panel (a) illustrate N_2 hydrogenation along consecutive (blue frames) and enzymatic (orange frames) paths, respectively. The small bubble and white balls in panel (a) indicate the N and H atoms, respectively, while the blue and orange larger balls represent the Mo and Sc atoms, respectively. The dashed line at zero in panel (c) represents the benchmark for N_2 adsorption preference. The solid line in panel (d) corresponds to $U_L = U_{HER}$, the limit below which eNRR will be more likely to occur, whereas the dashed line corresponds to $U_L - U_{HER} = -0.5$ V and eNRR domination, respectively.

ing. Furthermore, on h-MB surfaces, N_2 can be hydrogenated more easily along a mixed pathway ($^{**}N_2 \rightarrow$ **NNH $\rightarrow$ **NHNH $\rightarrow$ $^{**}NHNH_2$ $\rightarrow$ $^{*}NH^{*}NH_3$ $\rightarrow$ *NH $\rightarrow$ $^{*}NH_2$ $\rightarrow$ $^{*}NH_3$). The structures for the first step ($^{**}N_2$) in both configurations are shown in Figure S1. For the side-on configuration, N_2 adsorbs on the "hollow" site formed by the metal atoms with the N−N bond parallel to the B−B one. For the end-on configuration, N_2 adsorbs on top of the metal atoms. Because N_2 activation is a prerequisite for subsequent hydrogenation, the adsorption energies ΔE_{N2} of N_2 molecules at different sites were calculated, where * represents the adsorption sites. The results (shown in Figure S1 and listed in Table S3) first indicate that side-on-adsorbed N_2^{**} is energetically more favored.

Taking 2D MoB as an example, the calculated Gibbs free energy variations for the side-on and end-on reaction paths are depicted in Figure 2b. It is found that, on 2D MoB, N_2 will hydrogenate along the mixed pathway with a limiting potential (U_L) as low as −0.4 V. In particular, the extremely low energy barrier for the first hydrogenation ($^{**}N_2$ → **NNH) is a proof of the excellent N_2 activation ability of MoB. In fact, for most h-MBs, the potential-determining step (PDS) is one of the last two hydrogenation steps (*NH → $^{*}NH_2$ or $^{*}NH_2$ → $^{*}NH_3$), often leading to a rather low limiting potential (U_L) (Figure 2c). Taking the U_L of Ru(0001) as a reference,[9] six h-MB structures, VB, CrB, NbB, MoB, HfB, and WB, can be considered catalytically active for eNRR. In particular, 2D CrB, MoB, and WB display excellent catalytic activity with the U_L as low as −0.5 V, −0.4 V, and −0.56 V, respectively. It is worth mentioning that the M atoms constituting these stable h-MBs shown in Figure 2c are all early TMs. However, these data are insufficient to reflect the overall catalytic performance of h-MBenes.

To overcome this limitation and obtain a complete picture of the eNRR catalytic activity for h-MBs, a series of hypothetical h-MB phases were constructed by replacing M atoms with other transition metals of the periodic table and fully relaxing the structures. After structural optimization, AgB was distorted from a hexagonal to an orthorhombic symmetry. Besides, AuB, IrB, OsB, PtB, and ReB were distorted after N_2 adsorption, as shown in Figure S2. Given that the symmetry and the type of atomic packing dramatically influence the electron distribution in a given structure, the hypothetical MBs with significant distortions were excluded from the subsequent investigation. In total, the eNRR properties of 11 hypothetical h-MBs were studied, namely, YB, MnB, FeB, CoB, NiB, CuB, ZnB, CdB, PdB, RhB, and RuB.

The calculations show that the first hydrogenation ($^{**}N_2$ → **NNH) is uphill in energy for the post-TM h-MBs (Table S4) and that the activation of N_2 to NNH on those surfaces is more difficult than that on early-TM h-MBs. Interestingly, when combining the data of the stable and hypothetical h-MBs, a complete volcano-shaped relationship appears between the adsorption energy of NNH (ΔE_{NNH}) and U_L, as illustrated in Figure 2d. The closer these points representing different h-MBs are to the apex of the volcano curve, the higher their eNRR catalytic activity. Interestingly, h-MBs composed of early transition metals are all branched on the left, while h-MBs composed of post-TMs are mainly branched on the right, indicating the difference in the influence of early and post-TMs on the activation of nitrogen. Therefore, the volcano-shaped curve between the activity descriptor (ΔE_{NNH}) and U_L of

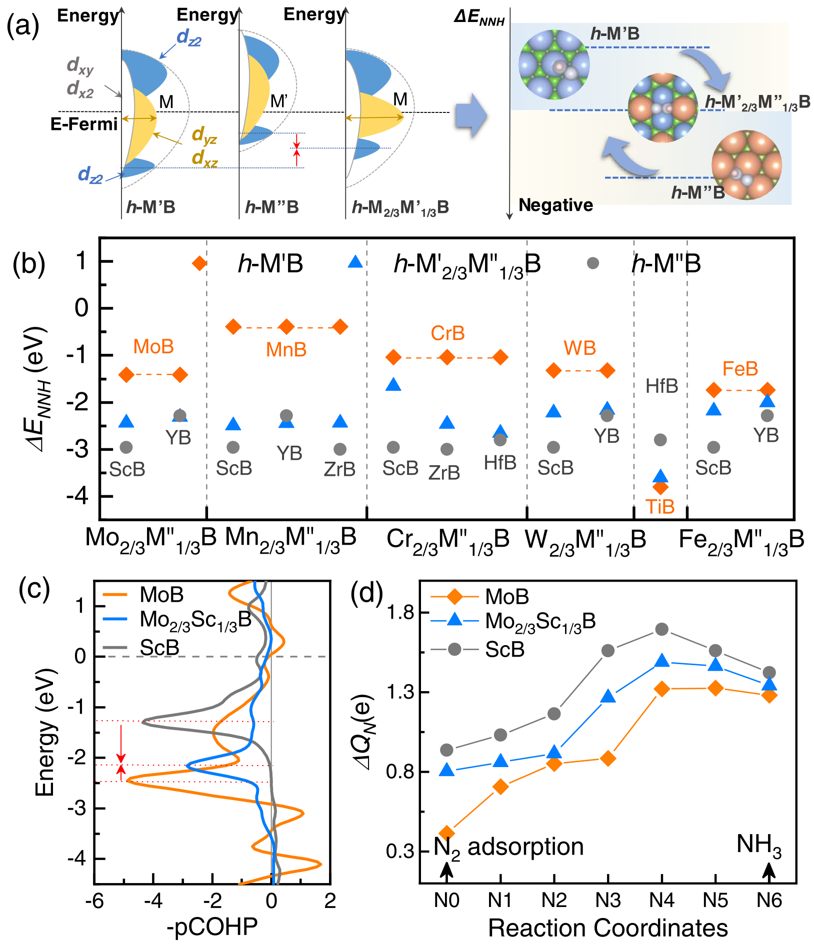

Figure 4. Effect of the alloying on the eNRR properties of h-$M'_{2/3}M''_{1/3}$Bs. (a) Schematic diagram of averaging of d_{z^2} orbitals for bimetallic h-$M'_{2/3}M''_{1/3}B$; (b) comparison of the calculated ΔE_{NNH} of h-$M'_{2/3}M''_{1/3}$Bs with those of the corresponding binary h-M′Bs and h-M″Bs; (c) calculated -pCOHP of 2D MoB, ScB, and $Mo'_{2/3}Sc''_{1/3}B$; (d) calculated charge transfer from the surface to N-containing groups (ΔQ_N) during six hydrogenation steps, where N0, N1, N2, N3, N4, N5, and N6 represents the $**N_2$, $**NNH$, $**NNH_2$, $*N$, $*NH$, $*NH_2$, and $*NH_3$ intermediates along the consecutive path for $Mo_{2/3}Sc_{1/3}B$ or $**N_2$, $**NNH$, $**NHNH$, $**NHNH_2$, $*NH$, $*NH_2$, and $*NH_3$ intermediates along the mixed path for MoB and ScB.

Figure 2d seems to provide a comprehensive understanding of the eNRR catalytic activity of 2D TM borides. This is not the case at all for the relationships between the adsorption energies of other N-containing intermediates (e.g., $*NH$, $*NH_2$, and $*NH_3$) and U_L, which are shown in Figure S3. Hence, the electrochemical stability of h-MBs was estimated by computing the corresponding Pourbaix diagrams (Figure S4). These indicate that the surfaces of all of the studied systems can be pristine upon applying a proper reduction potential. It is noteworthy that three h-MBs, CrB, MoB, and WB, can resist surface oxidation with a redox potential lower than −1.5 V and possess satisfactory eNRR catalytic activity. Furthermore, the calculated adsorption Gibbs free energies of N_2 and H_2O molecules on different h-MBs are reported in Figure S4(k), demonstrating that N_2 has a higher affinity for adsorption on the surface of h-MBs compared to H_2O. Such enhanced affinity can obviously facilitate the process of eNRR.

Previous works have already demonstrated that, in alloys[69] and single-atom alloys,[70,71] the Sabatier scaling relation can be overcome, leading to high activity and selectivity. In the family of 2D h-MBs, such an alloying can be obtained by introducing a second transition metal M″ with a ratio M′/M″ of 2:1 to form bimetallic 2D h-$M'_{2/3}M''_{1/3}B$. Indeed, high-throughput calculations have recently enabled the discovery of a variety of 2D h-$M'_{2/3}M''_{1/2}$Bs, including h-$Mo_{2/3}M''_{1/3}B$ (M″ = Sc and Y), h-$Mn_{2/3}M''_{1/3}B$ (M″ = Sc, Y and Zr), h-$Cr_{2/3}M''_{1/3}B$ (M″ = Sc, Zr and Hf), h-$W_{2/3}M''_{1/3}B$ (M″ = Sc and Y), h-$Fe_{2/3}M''_{1/3}B$ (M″ = Sc and Y), and h-$Ti_{2/3}Hf_{1/3}B$.[49,50] The two possible structures for h-$M'_{2/3}M''_{1/3}$Bs are shown in the left panel of Figure 1. Most h-$M'_{2/3}M''_{1/2}$Bs have the same structure as h-$Mo_{2/3}Sc_{1/3}B$,[28] which is the ternary h-MBene that was predicted first. It is illustrated at the right of the panel in Figure 1. However, previous theoretical works have demonstrated that h-$Fe_{2/3}M''_{1/3}$Bs adopt a different stacking structure, where the metal layers are mirrored with respect to the B layer as depicted in the center frame of the left panel of Figure 1.[45] Owing to their excellent stability and the diversity in the possible element combinations, h-$M'_{2/3}M''_{1/3}$Bs offer unparalleled prospects to improve the catalytic properties through bimetallic synergy.

In this work, the eNRR properties of h-$M'_{2/3}M''_{1/3}$Bs (M′ = Mo, Mn, Cr, W, and Fe; M″ = Sc, Y, Zr, and Hf) were thus studied by first carrying out Gibbs free energy calculations. As shown in Figure S5, there are two possible N_2 adsorption sites named S_1 and S_2 at the h-$M'_{2/3}M''_{1/3}B$ surfaces. Based on the calculated energies, the adsorption of N_2 is more likely to occur at S_1, a hollow site composed of two M′ and two M″, than at S_2. Therefore, in the subsequent calculations, we considered only the S_1 sites of h-$M'_{2/3}M''_{1/3}$Bs. N_2 tends to be reduced along the consecutive path, in which one N atom is first hydrogenated until it is reduced to NH_3 and then desorbed (Table S5). Figure 3a shows an example of the eNRR reaction pathways of h-$Mo_{2/3}Sc_{1/3}B$. The intermediates along the consecutive and enzymatic paths are displayed at the top and bottom of Figure 3a. The calculated U_L along the consecutive path is −0.56 V. Besides, just like for early h-MBs, the energy is reduced for the first hydrogenation step and the PDS is the last hydrogenation ($*NH_2 \rightarrow *NH_3$). Interestingly, the U_L of h-$M'_{2/3}M''_{1/3}B$ lies between those of the corresponding binary phases h-M′B and h-M″B (as shown in Figure 3b), slightly closer to that of h-M′B. For example, the U_L of h-$Mo_{2/3}Sc_{1/3}B$ (−0.56 V) is far from that of h-ScB (−1.15 V) and very close to that of h-MoB (−0.5 V). Therefore, most h-$M'_{2/3}M''_{1/3}$Bs display a high catalytic activity, with the notable exception of h-$Ti_{2/3}Hf_{1/3}B$, due to the inertness of both TiB and HfB on eNRR.

The hydrogen evolution reaction (HER) is an inevitable side reaction at the cathode, which usually results in a low yield and low Faraday efficiency during the preparation of NH_3. Therefore, besides high catalytic activity, selectivity is another important screening criterion to obtain the best eNRR catalysts. Therefore, the competition of the HER and eNRR on 2D borides was also studied, as shown in Figure 3c,d. Since the adsorption energy of N_2 or H on h-MBs reflects the binding strength between the reactants and the catalyst surfaces, the adsorption energy difference of N_2 and H on 2D borides ($\Delta G_{N_2} - \Delta G_H$) was first calculated to identify which molecules are most likely to occupy the reaction sites of the cathode (Figure 3c). All calculated energy differences (Figure 3c) are negative, which indicates that N_2 adsorption is energetically more favored than that of H. Notably, the bimetallic h-$M'_{2/3}M''_{1/3}B$ phases show much better eNRR selectivity than h-MBs. The selectivity for the formation of H_2 and NH_3 can be assessed by comparing the calculated limiting potentials of HER and eNRR (U_{HER} and U_L) (Figure 3d). For all of the hexagonal borides for which U_L is less negative than U_{HER} (i.e., all of the points located below the solid line in Figure 3d), eNRR will be dominating over HER (since it requires a smaller overpotential). This is the case for a number of binary h-MBs and ternary h-$M'_{2/3}M''_{1/3}$Bs, which hence possess excellent eNRR catalytic selectivity over HER. Furthermore, all other hexagonal borides fall below the dashed line $U_L - U_{HER} = -0.5$ V setting them in a better position than typical metals. Indeed, it has been previously shown that for the latter, the HER limiting potential requirements are consistently 0.5 V less negative than those for eNRR. [1515] The detailed data about catalytic selectivity are summarized in Table S6 in the Supporting Information.

The above results show that the catalytic activity and selectivity of the alloyed h-$M'_{2/3}M''_{1/3}$Bs can be improved compared to the pristine h-MB phases. To understand better the effect of alloying on the catalytic performance of 2D borides, detailed electronic structures were calculated. A few typical densities of states of pristine and alloyed phases are shown in Figure S6. Based on these calculations, the d_{z^2} orbitals of the 2D hexagonal boride are assumed to play a key role in tuning the eNRR properties. Indeed, taking h-MoB as an example, the calculations show that these orbitals are energetically close to the N_2 antibonding orbitals (Figure S7). And, by alloying, their energy range can be tuned to an average value between the pristine h-M′B and h-M″B (Figure S6). A favorable balance can thus be achieved between the effective dissociation of N_2 and the appropriate binding of the NH_X intermediates. These observations are consistent with the U_L values resulting from the Gibbs free energy calculations (Figure 3b). As illustrated in Figure 4a, the redistribution of d_{z^2} orbital energy levels as a result of the alloying thus determines the eNRR catalytic performance of 2D hexagonal borides.

In the above study of the eNRR properties of h-MBs, it was shown that ΔE_{NNH} and U_L are related through a volcano curve and that ΔE_{NNH} can thus be used as the main descriptor of the catalytic activity. Therefore, we first verified that U_L and ΔE_{NNH} satisfy the same volcano-shaped relationship for h-$M'_{2/3}M''_{1/3}$Bs (Figure S8). In fact, as shown in Figure 4b, the calculated values of ΔE_{NNH} for h-$M'_{2/3}M''_{1/3}$Bs are between those of h-M′B and h-M″B just as the values of U_L. Taking h-$Mo_{2/3}Sc_{1/3}B$ as an example, the bonding conditions of **NNH with 2D $Mo_{2/}Sc_{1/3}B$, MoB, and ScB were studied by calculating the projected crystal orbital Hamiltonian population (pCOHP) of the structures with **NNH groups adsorbed. In h-$Mo_{2/}Sc_{1/3}B$, the antibonding state of the interaction of **NNH with the surface is shifted upward compared with that at MoB, which is lower than that at 2D ScB (Figure 4c). Because the chemical reaction process is a redistribution process of valence electrons, the charge transfer from the 2D $Mo_{2/}Sc_{1/3}B$, MoB, and ScB surface to adsorbed N-containing groups (ΔQ_N) was calculated and the results satisfy the averaging effect as shown in Figure 4d.

These theoretical results indicate that the averaging of the d_{z^2} orbital positions is reflected in the change in Gibbs free energy and the bonding of N-containing groups with the surfaces. This suggests that ΔE_{NNH} would be a suitable descriptor for the catalytic performance of h-$M'_{2/3}M''_{1/3}$Bs. Indeed, the calculated values of U_L and ΔE_{NNH} for h-$M'_{2/3}M''_{1/3}$Bs also satisfy the volcano-shaped relationship (Figure S8), demonstrating the good transferability of the catalytic descriptor ΔE_{NNH}. Besides, most points are close to the peak of the volcano curve, indicating the promotion of eNRR catalytic activity after alloying.

Although the eNRR catalytic performance of 2D borides can be engineered through the construction of h-$M'_{2/3}M''_{1/3}$Bs by using two kinds of transition metals, the number of energetically favored h-$M'_{2/3}M''_{1/3}$Bs is limited. Indeed, a former study has revealed that the ratio of M′ and M″ is fixed and the atomic radius of M″ should be larger than that of M′ by at least 0.2 Å to ensure the stability.[49] Besides the formation of bimetallic 2D h-$M'_{2/3}M''_{1/3}$Bs, it is remarkable that heteroatom alloying during exfoliation or postprocessing can be achieved, hence modifying the catalytic properties of h-MBenes.[26,72] This can generate multiple structures using different alloying elements and variable alloying concentration.[71] Therefore, alloying provides a feasible way for tuning the catalytic properties of binary h-MBs, which was implemented in the following study. In addition, the idea of utilizing high entropy alloys opens up more degrees of freedom to fine-tune the composition of the alloy,[73] aiming at the desired properties and performance. This approach has been demonstrated to be successful in previous studies and holds the potential for preparing $M'_{8/9}M''_{1/9}B$ with controlled ratios of the two metals. Further exploration and experimentation in this direction could yield promising results.

Referring to the volcano-shaped diagram shown in Figure S7, 2D WB ($U_L = -0.56$ V) and NbB ($U_L = -0.74$ V) on the

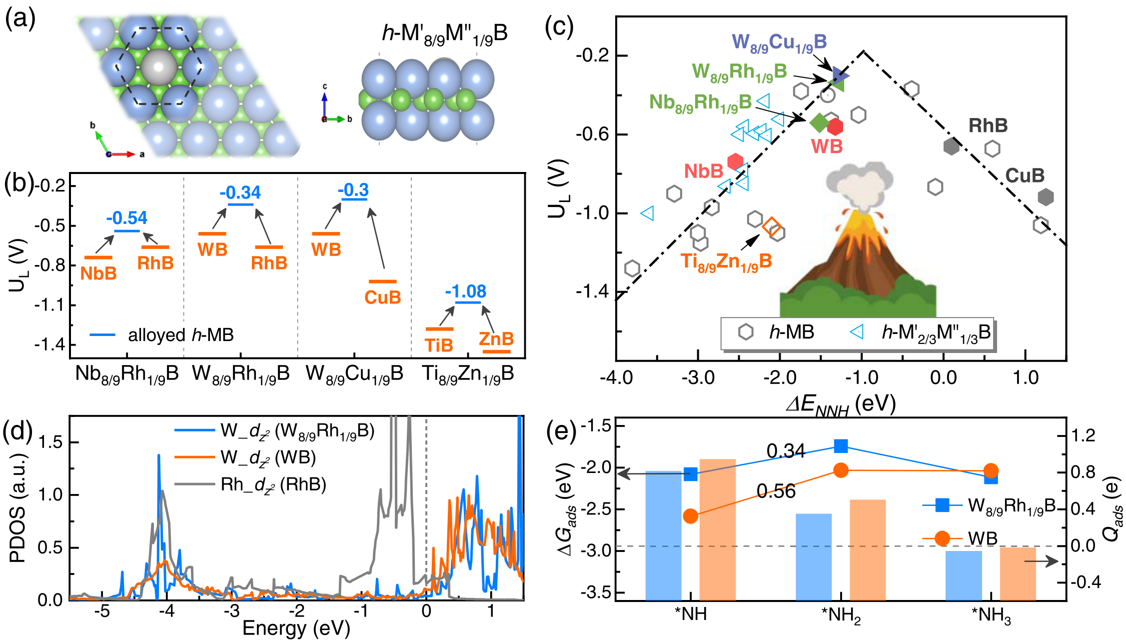

Figure 5. Catalytic activities and electronic structures of second transition metal alloyed *h*-MBene phases: (a) structure of *h*-$MB'_{8/9}M''_{1/9}B$; (b) calculated U_L of *h*-$M_{8/9}M''_{1/9}B$ in comparison with those of their parent *h*-MB phases; (c) volcano-shaped curve between ΔE_{NNH} and U_L, using the data of all h-MBene structures studied in this work; (d) calculated PDOS of W_d_{z^2} of $W_{8/9}Rh_{1/9}B$, W_d_{z^2} of WB and Rh_d_{z^2} of $W_{8/9}Rh_{1/9}B$; (e) calculated adsorption Gibbs free energies of *NH, $*NH_2$, and $*NH_3$ and the corresponding charge transfers between 2D $W_{8/9}Rh_{1/9}B$ and these intermediates. Positive and negative values of Q_{ads} represent charge transfer from the surface to the intermediate and charge transfer from the intermediate to the surface, respectively.

left branch, which can represent eNRR catalysts with high and medium catalytic activities, respectively, were selected as the solid crystalline foundations for alloying. Besides, considering the averaging effect of transition metals, Rh was chosen as the alloying element because of the symmetric position of RhB (U_L = −0.66 V) on the right branch compared with that of WB and NbB in Figure S8. In addition, Cu-alloyed WB and Zn-alloyed TiB were studied due to the abundance of these two elements. Structures with a high alloying concentration of 1/3 and low concentration of 1/9 were constructed, which are expressed as $M'_{2/3}M''_{1/3}B$ and $M'_{8/9}M''_{1/9}B$, respectively.

The structures of Rh-alloyed 2D WB and NbB with high alloying concentrations ($W_{2/3}Rh_{1/3}B$ and $Nb_{2/3}Rh_{1/3}B$) were first constructed and studied. Our target was that the M′−M″ alloy could inherit from the advantages of *h*-M′B and *h*-M″B, namely, the high N_2 activation degree of *h*-M′B composed of early transition metals (W and Nb) and the mild reaction process of *h*-M″B composed of post-transition metals (Rh and Cu). However, the results show that the calculated U_L values of $W_{2/3}Rh_{1/3}B$ (−0.51 V) and $Nb_{2/3}Rh_{1/3}B$ (−0.74 V) are comparable with those of WB and NbB (Figure S9). Therefore, we concluded that a high alloying concentration is not a suitable strategy to improve the eNRR properties of *h*-MBs. We thus investigated the effect of a low alloying concentration of 1/9 for WB and NbB. The results are shown in Figure 5. In the alloy structure, the alloying atom M″ is coordinated by six matrix M′ atoms to form a hexagonal alloying region (Figure 5a). The calculations show that N_2 adsorbs adopting the side-on configuration at the hollow sites surrounded by three M′ and one M″ atoms (Figure S10). Interestingly, the catalytic activities of 2D $M'_{8/9}M''_{1/9}B$ structures can be promoted significantly as shown in Figure 5b. Detailed data are summarized in Table S7. The studied 2D $Nb_{8/9}Rh_{1/8}B$, $W_{8/9}Rh_{1/9}B$, and $W_{8/9}Cu_{1/9}B$ structures have a value of U_L as low as −0.54 V, −0.34 V, and −0.3 V. By combining the calculated data of U_L and ΔE_{NNH} of all binary and alloyed *h*-MBenes, a complete volcano-shaped curve was produced as shown in Figure 5c. The positions of the alloyed *h*-$M'_{8/9}M''_{1/9}B$ structures are all closer to the peak of the volcano-shaped curve than those of their parent *h*-MB phases. This demonstrates the feasibility of designing and generating better eNRR catalysts by heteroalloying thanks to the volcano-shaped relationship of U_L and ΔE_{NNH}. Surprisingly, the Cu-alloyed 2D WB structure, $W_{8/9}Cu_{1/9}B$, shows even superior properties compared to the other studied structures, demonstrating the possibility to obtain excellent eNRR catalysts using earth-abundant elements. For the Zn-alloyed TiB, the calculated U_L of 2D $Ti_{8/9}Zn_{1/9}B$ (U_L = −1.08 V) is, however, lower than that of the bare TiB (U_L = −1.28 V): the increased catalytic activity cannot overcome the inertness of TiB itself. Therefore, the catalytic performance of the alloyed structure is jointly determined by the type of alloying element and the intrinsic catalytic activity of pristine *h*-MBs.

In order to analyze the bimetallic alloying effect, the electronic structures of 2D WB and NbB before and after Rh alloying were studied in detail (Figure S11). There is a significant overlap of the *d* orbitals between Rh and W below the Fermi energy, especially for the d_{z^2} orbitals near −3.5 eV. These can jointly regulate the activation degree of N_2 and intermediates as shown in Figure 5d. From the point of view of the scaling relationship, a strong activation of N_2 can inhibit the subsequent reduction process of eNRR. Bader Charge analysis shows that bimetallic alloying triggers charge transfer from W (or Nb) to Rh (Table S8), thereby reducing the electron density around W (or Nb) (Figure S12). Figure 5e shows the charge transfers from the surface to the NH_x (x = 1, 2 and 3) intermediates and the corresponding adsorption energies of the NH_x molecules on the $W_{8/9}Rh_{1/9}B$ surface,

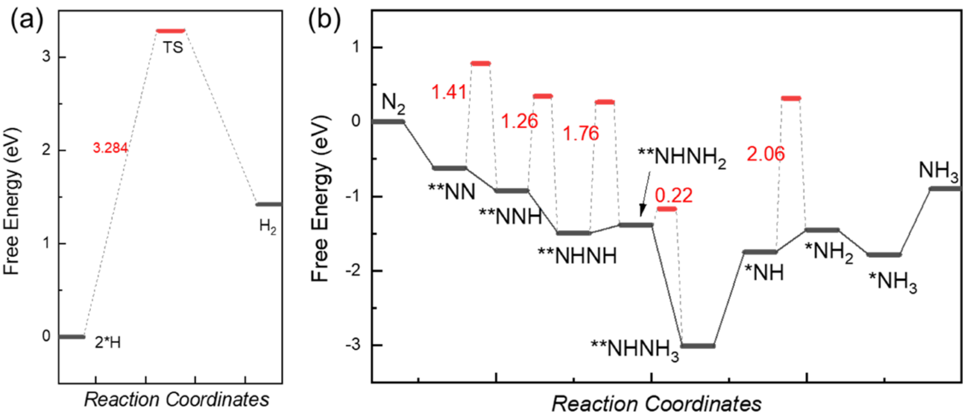

Figure 6. Reaction paths of HER (a) and eNRR (b) on the surface of $W_{8/9}Cu_{1/9}B$. The red solid bars indicate the calculated kinetic barriers.

expressed with respect to those on the bare 2D WB. The introduction of Rh into the 2D WB reduces the charge transfer to W and Rh as well as to the intermediates, thus promoting the smooth progress of the reaction. The same results were found after Rh-alloyed NbB was formed (Figure S13). Moreover, the charge transfer between the intermediates and the 2D surfaces (Q_{ads}, e) and the corresponding limiting potentials show a linear relationship (Figure S14). This suggests that transferring fewer electrons from the *h*-MBene surface is favorable for the progress of eNRR. In addition to the influence of thermodynamic factors on eNRR catalytic activity, finally, to assess the reaction kinetics, the energy barriers of every step of both HER and eNRR on the surface of $W_{8/9}Cu_{1/9}B$, which possesses the lowest U_L (−0.3 V) among all of the studied structures, were calculated using CI-NEB (Figure 6). The results show that the formation of H_2 from adsorbed H on the $W_{8/9}Cu_{1/9}B$ surface is quite difficult with an energy barrier as high as 3.28 eV (Figure 6a). In comparison, the highest kinetic barrier for the eNRR process on the $W_{8/9}Cu_{1/9}B$ surface is only 2.06 eV, which is much lower than that for HER (Figure 6b). Therefore, one can conclude that from the reaction kinetics standpoint, eNRR is also preferred over HER on the $W_{8/9}Cu_{1/9}B$ surface.

4. CONCLUSIONS

In this work, the eNRR properties of a series of 2D *h*-MBenes were systematically investigated. Based on their catalytic activity and selectivity, 6 *h*-MBs and 11 *h*-$M'_{2/3}M''_{1/3}$Bs were screened out as excellent candidates for eNRR catalysis. In particular, 2D CrB, MoB, and WB and their corresponding in-plane ordered phases, *h*-$Cr_{2/3}M''_{1/3}B$, *h*-$Mo_{2/3}M''_{1/3}B$, and *h*-$W_{2/3}M''_{1/3}B$, display a limiting potential U_L lower than −0.6 V. It was demonstrated that the adsorption energy of **NNH can be a suitable descriptor for the performance of *h*-MBenes. By analyzing the calculated Gibbs free energies and electronic structures, an explanation was proposed for the catalytic activity of 2D *h*-MBenes: the energy redistribution of d_{z^2} orbitals transition metals during alloying can ensure the smooth activation of N_2 and N-containing intermediates in a proper range, consequently breaking the scaling relationship. Moreover, guided by the constructed volcano-shaped curve for the *h*-MBene eNRR activity and by the proposed averaging mechanism, a series of bimetallic 2D borides was designed with superior eNRR catalytic activity, resulting from the insertion of a second transition metal. In particular, the proposed 2D $W_{8/9}Cu_{1/9}B$, which is only composed of earth-abundant transition metals, possesses a limiting potential U_L as low as −0.30 V. This work has revealed the great potential of *h*-MBenes as green eNRR electrocatalysts, which will stimulate the enthusiasm of researchers in the electrochemical studies and applications of *h*-MBenes.

■ ASSOCIATED CONTENT

Supporting Information

The Supporting Information is available free of charge at https://pubs.acs.org/doi/10.1021/acs.chemmater.3c01656.

> Theoretical Calculations about Pourbaix diagram; N_2 adsorption, eNRR descriptors, and electrochemical stability of *h*-MBs; N_2 adsorption, electronic structures and eNRR descriptors of *h*-$M'_{2/3}M''_{1/3}$Bs; eNRR activity, N_2 adsorption, and electronic structures for *h*-$M'_{8/9}M''_{1/9}$Bs; tables of eNRR data for *h*-MBs, *h*-$M'_{2/3}M''_{1/3}$Bs, and *h*-$M'_{8/9}M''_{1/9}$Bs (PDF)

■ AUTHOR INFORMATION

Corresponding Author

Junjie Wang − *State Key Laboratory of Solidification Processing, Northwestern Polytechnical University, Xi'an, Shaanxi 710072, People's Republic of China;* orcid.org/0000-0002-6428-2233; Email: wang.junjie@nwpu.edu.cn

Authors

Shuang Feng − *State Key Laboratory of Solidification Processing, Northwestern Polytechnical University, Xi'an, Shaanxi 710072, People's Republic of China; CATARC (Tianjin) Automotive Engineering Research Institute Co., Ltd., Tianjin 300300, People's Republic of China*

Yufang Yao − *State Key Laboratory of Solidification Processing, Northwestern Polytechnical University, Xi'an, Shaanxi 710072, People's Republic of China*

Jean-Christophe Charlier − *Institute of Condensed Matter and Nanosciences, UCLouvain, Louvain-la-Neuve 1348, Belgium*

Gian-Marco Rignanese − *State Key Laboratory of Solidification Processing, Northwestern Polytechnical University, Xi'an, Shaanxi 710072, People's Republic of China; Institute of Condensed Matter and Nanosciences, UCLouvain, Louvain-la-Neuve 1348, Belgium;* orcid.org/0000-0002-1422-1205

Complete contact information is available at: https://pubs.acs.org/10.1021/acs.chemmater.3c01656

Notes

The authors declare no competing financial interest.

■ ACKNOWLEDGMENTS

This work was supported by the National Key Research and Development Program of Intergovernmental Cooperation in Science and Technology (Grant No. 2022YFE0141100), the National Natural Science Foundation of China (Grant No. 52272307) and the Fundamental Research Funds for the Central Universities (No. D5000220172).

■ REFERENCES

(1) Valera-Medina, A.; Xiao, H.; Owen-Jones, M.; David, W. I. F.; Bowen, P. J. Ammonia for power. *Prog. Energy Combust. Sci.* **2018**, *69*, 63−102.

(2) Vojvodic, A.; Medford, A. J.; Studt, F.; Abild-Pedersen, F.; Khan, T. S.; Bligaard, T.; Nørskov, J. K. Exploring the limits: A low-pressure, low-temperature Haber−Bosch process. *Chem. Phys. Lett.* **2014**, *598*, 108−112.

(3) Erisman, J. W.; Sutton, M. A.; Galloway, J.; Klimont, Z.; Winiwarter, W. How a century of ammonia synthesis changed the world. *Nat. Geosci.* **2008**, *1*, 636−639.

(4) Rostrup-Nielsen, J. R.; Rostrup-Nielsen, T. Large-Scale Hydrogen Production. *Cattech* **2002**, *6*, 150−159.

(5) Martín, A. J.; Shinagawa, T.; Pérez-Ramírez, J. Electrocatalytic Reduction of Nitrogen: From Haber-Bosch to Ammonia Artificial Leaf. *Chem* **2019**, *5*, 263−283.

(6) Pickett, C. J.; Talarmin, J. Electrosynthesis of ammonia. *Nature* **1985**, *317*, 652−653.

(7) Sippel, D.; Rohde, M.; Netzer, J.; Trncik, C.; Gies, J.; Grunau, K.; Djurdjevic, I.; Decamps, L.; Andrade, S. L. A.; Einsle, O. A bound reaction intermediate sheds light on the mechanism of nitrogenase. *Science* **2018**, *359*, 1484−1489.

(8) Kordali, V.; Kyriacou, G.; Lambrou, C. Electrochemical synthesis of ammonia at atmospheric pressure and low temperature in a solid polymer electrolyte cell. *Chem. Commun.* **2000**, 1673−1674.

(9) Skúlason, E.; Bligaard, T.; Gudmundsdottir, S.; Studt, F.; Rossmeisl, J.; Abild-Pedersen, F.; Vegge, T.; Jonsson, H.; Norskov, J. K. A theoretical evaluation of possible transition metal electrocatalysts for N2 reduction. *Phys. Chem. Chem. Phys.* **2012**, *14*, 1235−1245.

(10) Gong, Y.; Wu, J.; Kitano, M.; Wang, J.; Ye, T.-N.; Li, J.; Kobayashi, Y.; Kishida, K.; Abe, H.; Niwa, Y.; Yang, H.; Tada, T.; Hosono, H. Ternary intermetallic LaCoSi as a catalyst for N_2 activation. *Nat. Catal.* **2018**, *1*, 178−185.

(11) Pool, J. A.; Lobkovsky, E.; Chirik, P. J. Hydrogenation and cleavage of dinitrogen to ammonia with a zirconium complex. *Nature* **2004**, *427*, 527−530.

(12) Chu, K.; Li, X.; Li, Q.; Guo, Y.; Zhang, H. Synergistic Enhancement of Electrocatalytic Nitrogen Reduction Over Boron Nitride Quantum Dots Decorated Nb_2CTx -MXene. *Small* **2021**, *17*, No. e2102363.

(13) Kour, G.; Mao, X.; Du, A. Computational screening of single-atom alloys TM@Ru(0001) for enhanced electrochemical nitrogen reduction reaction. *J. Mater. Chem. A* **2022**, *10*, 6204−6215.

(14) Back, S.; Jung, Y. On the mechanism of electrochemical ammonia synthesis on the Ru catalyst. *Phys. Chem. Chem. Phys.* **2016**, *18*, 9161−9167.

(15) Montoya, J. H.; Tsai, C.; Vojvodic, A.; Norskov, J. K. The Challenge of Electrochemical Ammonia Synthesis: A New Perspective on the Role of Nitrogen Scaling Relations. *ChemSusChem* **2015**, *8*, 2180−2186.

(16) Singh, A. R.; Rohr, B. A.; Schwalbe, J. A.; Cargnello, M.; Chan, K.; Jaramillo, T. F.; Chorkendorff, I.; Nørskov, J. K. Electrochemical Ammonia Synthesis—The Selectivity Challenge. *ACS Catal.* **2017**, *7*, 706−709.

(17) van der Ham, C. J. M.; Koper, M. T.; Hetterscheid, D. G. Challenges in reduction of dinitrogen by proton and electron transfer. *Chem. Soc. Rev.* **2014**, *43*, 5183−5191.

(18) Geng, Z.; Liu, Y.; Kong, X.; Li, P.; Li, K.; Liu, Z.; Du, J.; Shu, M.; Si, R.; Zeng, J. Achieving a Record-High Yield Rate of 120.9 mugNH$_3$ mgcat.$^{-1}$ h^{-1} for N_2 Electrochemical Reduction over Ru Single-Atom Catalysts. *Adv. Mater.* **2018**, *30*, No. e1803498.

(19) Qian, Y.; Liu, Y.; Zhao, Y.; Zhang, X.; Yu, G. Single vs double atom catalyst for N_2 activation in nitrogen reduction reaction: A DFT perspective. *EcoMat* **2020**, *2*, No. e12014.

(20) Xu, Z.; Ao, Z.; Yang, M.; Wang, S. Recent progress in single-atom alloys: Synthesis, properties, and applications in environmental catalysis. *J. Hazard. Mater.* **2022**, *424*, No. 127427.

(21) Augustyn, V.; Gogotsi, Y. 2D Materials with Nanoconfined Fluids for Electrochemical Energy Storage. *Joule* **2017**, *1*, 443−452.

(22) Yang, S.; Zhang, P.; Nia, A. S.; Feng, X. Emerging 2D Materials Produced via Electrochemistry. *Adv. Mater.* **2020**, *32*, No. e1907857.

(23) Geim, A. K. Graphene: Status and Prospects. *Science* **2009**, *324*, 1530−1534.

(24) Li, J.; Zhang, Y.; Liu, C.; Zheng, L.; Petit, E.; Qi, K.; Zhang, Y.; Wu, H.; Wang, W.; Tiberj, A.; Wang, X.; Chhowalla, M.; Lajaunie, L.; Yu, R.; Voiry, D. 3.4% Solar-to-Ammonia Efficiency from Nitrate Using Fe Single Atomic Catalyst Supported on MoS_2Nanosheets. *Adv. Funct. Mater.* **2021**, No. 2108316.

(25) Ma, Z.; Xiao, C.; Cui, Z.; Du, W.; Li, Q.; Sa, R.; Sun, C. Defective Fe3GeTe2 monolayer as a promising electrocatalyst for spontaneous nitrogen reduction reaction. *J. Mater. Chem. A* **2021**, *9*, 6945−6954.

(26) Peng, W.; Luo, M.; Xu, X.; Jiang, K.; Peng, M.; Chen, D.; Chan, T. S.; Tan, Y. Spontaneous Atomic Ruthenium Doping in Mo2CTx MXene Defects Enhances Electrocatalytic Activity for the Nitrogen Reduction Reaction. *Adv. Energy Mater.* **2020**, *10*, 2001364−2001374.

(27) Sun, C.; Chen, Z.; Cui, J.; Li, K.; Qu, H.; Xie, H.; Zhong, Q. Site-exposed Ti_3C_2 MXene anchored in N-defect g-C3N4 heterostructure nanosheets for efficient photocatalytic N_2 fixation. *Catal. Sci. Technol.* **2021**, *11*, 1027−1038.

(28) Wang, S.; Li, B.; Li, L.; Tian, Z.; Zhang, Q.; Chen, L.; Zeng, X. C. Highly efficient N_2 fixation catalysts: transition-metal carbides M_2C (MXenes). *Nanoscale* **2020**, *12*, 538−547.

(29) Zhou, A.; Liu, Y.; Li, S.; Wang, X.; Ying, G.; Xia, Q.; Zhang, P. From structural ceramics to 2D materials with multi-applications: A review on the development from MAX phases to MXenes. *J. Adv. Ceram.* **2021**, *10*, 1194−1242.

(30) Zhang, T.; Zhang, B.; Peng, Q.; Zhou, J.; Sun, Z. Mo_2B_2 MBene-supported single-atom catalysts as bifunctional HER/OER and OER/ORR electrocatalysts. *J. Mater. Chem. A* **2021**, *9*, 433−441.

(31) Bo, T.; Liu, P. F.; Xu, J.; Zhang, J.; Chen, Y.; Eriksson, O.; Wang, F.; Wang, B. T. Hexagonal Ti2B2 monolayer: a promising anode material offering high rate capability for Li-ion and Na-ion batteries. *Phys. Chem. Chem. Phys.* **2018**, *20*, 22168−22178.

(32) Wang, S.; Khazaei, M.; Wang, J.; Hosono, H. Hypercoordinate two-dimensional transition-metal borides for spintronics and catalyst applications. *J. Mater. Chem. C* **2021**, *9*, 9212−9221.

(33) Wang, S.; Miao, N.; Su, K.; Blatov, V. A.; Wang, J. Discovery of intrinsic two-dimensional antiferromagnets from transition-metal borides. *Nanoscale* **2021**, *13*, 8254−8263.

(34) Zhang, B.; Zhou, J.; Elliott, S. R.; Sun, Z. Two-dimensional molybdenum carbides: active electrocatalysts for the nitrogen reduction reaction. *J. Mater. Chem. A* **2020**, *8*, 23947−23954.

(35) Guo, Z. L.; Zhou, J.; Sun, Z. New Two-dimensional Transition Metal Borides for Li ion Batteries and Electrocatalysis. *J. Mater. Chem. A* **2017**, *5*, 23530−23535.

(36) Wang, E.; Zhang, B.; Zhou, J.; Sun, Z. High catalytic activity of MBenes-supported single atom catalysts for oxygen reduction and oxygen evolution reaction. *Appl. Surf. Sci.* **2022**, *604*, No. 154522.

(37) Gao, Y.; Wang, E.; Zheng, Y.; Zhou, J.; Sun, Z. Hexagonal MBenes-Supported Single Atom as Electrocatalysts for the Nitrogen Reduction Reaction. *Energy Mater. Adv.* **2023**, *4*, No. 0039.

(38) Zhang, B.; Zhou, J.; Sun, Z. MBenes: progress, challenges and future. *J. Mater. Chem. A* **2022**, *10*, 15865−15880.

(39) Sharma, A.; Rangra, V. S.; Thakur, A. Synthesis, properties, and applications of MBenes (two-dimensional metal borides) as emerging 2D materials: a review. *J. Mater. Sci.* **2022**, *57*, 12738−12751.

(40) Yao, M.; Shi, Z.; Zhang, P.; Ong, W.-J.; Jiang, J.; Ching, W.-Y.; Li, N. Density Functional Theory Study of Single Metal Atoms Embedded into MBene for Electrocatalytic Conversion of N2 to NH3. *ACS Appl. Nano Mater.* **2020**, *3*, 9870−9879.

(41) Xiao, Y.; Shen, C.; Long, T. Theoretical Establishment and Screening of an Efficient Catalyst for N_2 Electroreduction on Two-Dimensional Transition-Metal Borides (MBenes). *Chem. Mater.* **2021**, *33*, 4023−4034.

(42) Guo, X.; Lin, S.; Gu, J.; Zhang, S.; Chen, Z.; Huang, S. Establishing a Theoretical Landscape for Identifying Basal Plane Active 2D Metal Borides (MBenes) toward Nitrogen Electroreduction. *Adv. Funct. Mater.* **2020**, *31*, No. 2008056.

(43) Nair, V. G.; Birowska, M.; Bury, D.; Jakubczak, M.; Rosenkranz, A.; Jastrzebska, A. M. 2D MBenes: A Novel Member in the Flatland. *Adv. Mater.* **2022**, *34*, No. e2108840.

(44) Wang, J.; Ye, T. N.; Gong, Y.; Wu, J.; Miao, N.; Tada, T.; Hosono, H. Discovery of hexagonal ternary phase Ti2InB2 and its evolution to layered boride TiB. *Nat. Commun.* **2019**, *10*, No. 2284.

(45) Miao, N.; Wang, J.; Gong, Y.; Wu, J.; Niu, H.; Wang, S.; Li, K.; Oganov, A. R.; Tada, T.; Hosono, H. Computational Prediction of Boron-Based MAX Phases and MXene Derivatives. *Chem. Mater.* **2020**, *32*, 6947−6957.

(46) Ade, M.; Hillebrecht, H. Ternary Borides Cr2AlB2, Cr3AlB4, and Cr4AlB6: The First Members of the Series (CrB_2)nCrAl with n = 1, 2, 3 and a Unifying Concept for Ternary Borides as MAB-Phases. *Inorg. Chem.* **2015**, *54*, 6122−6135.

(47) Khazaei, M.; Wang, J.; Estili, M.; Ranjbar, A.; Suehara, S.; Arai, M.; Esfarjani, K.; Yunoki, S. Novel MAB phases and insights into their exfoliation into 2D MBenes. *Nanoscale* **2019**, *11*, 11305−11314.

(48) Khaledialidusti, R.; Khazaei, M.; Wang, V.; Miao, N.; Si, C.; Wang, J.; Wang, J. Exploring structural, electronic, and mechanical properties of 2D hexagonal MBenes. *J. Phys.: Condens. Matter* **2021**, 33, No. 155503.

(49) Dahlqvist, M.; Petruhins, A.; Lu, J.; Hultman, L.; Rosen, J. Origin of Chemically Ordered Atomic Laminates (i-MAX): Expanding the Elemental Space by a Theoretical/Experimental Approach. *ACS Nano* **2018**, *12*, 7761−7770.

(50) Dahlqvist, M.; Rosen, J. Predictions of attainable compositions of layered quaternary i-MAB phases and solid solution MAB phases. *Nanoscale* **2021**, *13*, 18311−18321.

(51) Yao, Y.; Miao, N.; Gong, Y.; Wang, J. Theoretical exploration of quaternary hexagonal MAB phases and two-dimensional derivatives. *Nanoscale* **2021**, *13*, 13208−13214.

(52) Lind, H.; Dahlqvist, M.; Rosen, J. In-plane ordered quaternary M4/3′M2/3″AlB2 phases (i-MAB): electronic structure and mechanical properties from first-principles calculations. *J. Phys.: Condens. Matter* **2021**, *33*, No. 255402.

(53) Dahlqvist, M.; Tao, Q.; Zhou, J.; Palisaitis, J.; Persson, P. O. A.; Rosen, J. Theoretical Prediction and Synthesis of a Family of Atomic Laminate Metal Borides with In-Plane Chemical Ordering. *J. Am. Chem. Soc.* **2020**, *142*, 18583−18591.

(54) Hanner, L. A.; Badr, H. O.; Dahlqvist, M.; Kota, S.; Raczkowski, D.; Rosen, J.; Barsoum, M. W. Synthesis, characterization and first principle modelling of the MAB phase solid solutions: (Mn1-xCrx)2AlB2 and (Mn1-xCrx)3AlB4. *Mater. Res. Lett.* **2021**, *9*, 112−118.

(55) Sun, Y.; Wang, G.; Li, K.; Peng, L.; Zhou, J.; Sun, Z. Accelerating the Discovery of Transition Metal Borides by Machine Learning on Small Data Sets. *ACS Appl. Mater. Interfaces* **2023**, *15*, 29278−29286.

(56) Zhou, J.; Palisaitis, J.; Halim, J.; Dahlqvist, M.; Tao, Q.; Persson, I.; Hultman, L.; Persson, P. O. Å.; Rosen, J. Boridene: Two-dimensional Mo4/3B2-x with ordered metal vacancies obtained by chemical exfoliation. *Science* **2021**, *373*, 801−805.

(57) Miao, N.; Gong, Y.; Zhang, H.; Shen, Q.; Yang, R.; Zhou, J.; Hosono, H.; Wang, J. Discovery of Two-dimensional Hexagonal MBene HfBO and Exploration on its Potential for Lithium-Ion Storage. *Angew. Chem., Int. Ed.* **2023**, *62*, No. e202308436.

(58) Blöchl, P. E. Projector augmented-wave method. *Phys. Rev. B.: Condens. Matter.* **1994**, *50*, 17953−17979.

(59) Kresse, G.; Furthmüller, J. Efficiency of ab-initio total energy calculations for metals and semiconductors using a plane-wave basis set. *Comput. Mater. Sci.* **1996**, *6*, 15−50.

(60) Kresse, G.; Furthmüller, J. Efficient iterative schemes for ab initio total-energy calculations using a plane-wave basis set. *Phys. Rev. B* **1996**, *54*, 11169−11186.

(61) Perdew, J. P.; Wang, Y. Accurate and simple analytic representation of the electron-gas correlation energy. *Phys. Rev. B: Condens. Matter* **1992**, *45*, 13244−13249.

(62) Grimme, S.; Antony, J.; Ehrlich, S.; Krieg, H. A consistent and accurate ab initio parametrization of density functional dispersion correction (DFT-D) for the 94 elements H-Pu. *J. Chem. Phys.* **2010**, *132*, No. 154104.

(63) Deringer, V. L.; Tchougréeff, A. L.; Dronskowski, R. Crystal Orbital Hamilton Population (COHP) Analysis As Projected from Plane-Wave Basis Sets. *J. Phys. Chem. A* **2011**, *115*, 5461−5466.

(64) Dronskowski, R.; Blöchl, P. E. Crystal orbital Hamilton populations (COHP): energy-resolved visualization of chemical bonding in solids based on density-functional calculations. *J. Phys. Chem. A* **1993**, *97*, 8617−8624.

(65) Wang, V.; Xu, N.; Liu, J. C.; Tang, G.; Geng, W. J. C. P. C. VASPKIT: A user-friendly interface facilitating high-throughput computing and analysis using VASP code. *Comput. Phys. Commun.* **2021**, *267*, No. 108033.

(66) Momma, K.; Izumi, F. VESTA 3for three-dimensional visualization of crystal, volumetric and morphology data. *J. Appl. Crystallogr.* **2011**, *44*, 1272−1276.

(67) Nørskov, J. K.; Rossmeisl, J.; Logadottir, A.; Lindqvist, L.; Kitchin, J. R.; Bligaard, T.; Jónsson, H. Origin of the Overpotential for Oxygen Reduction at a Fuel-Cell Cathode. *J. Phys. Chem. B* **2004**, *108*, 17886−17892.

(68) Shipman, M. A.; Symes, M. D. Recent progress towards the electrosynthesis of ammonia from sustainable resources. *Catal. Today* **2017**, *286*, 57−68.

(69) Gong, Y.; Li, H.; Li, C.; Yang, X.; Wang, J.; Hosono, H. LaRuSi Electride Disrupts the Scaling Relations for Ammonia Synthesis. *Chem. Mater.* **2022**, *34*, 1677−1685.

(70) Li, X.; Shen, P.; Luo, Y.; Li, Y.; Guo, Y.; Zhang, H.; Chu, K. PdFe Single-Atom Alloy Metallene for N2 Electroreduction. *Angew. Chem., Int. Ed.* **2022**, *61*, No. e202205923.

(71) Wei, C.; Sun, Y.; Scherer, G. G.; Fisher, A. C.; Sherburne, M.; Ager, J. W.; Xu, Z. J. Surface Composition Dependent Ligand Effect in Tuning the Activity of Nickel-Copper Bimetallic Electrocatalysts toward Hydrogen Evolution in Alkaline. *J. Am. Chem. Soc.* **2020**, *142*, 7765−7775.

(72) Ibragimova, R.; Rinke, P.; Komsa, H.-P. Native Vacancy Defects in MXenes at Etching Conditions. *Chem. Mater.* **2022**, *34*, 2896−2906.

(73) Xu, H.; Jiang, L.; Chen, K.; Huang, Q.; Zhou, X. High-entropy rare-earth diborodicarbide: A novel class of high-entropy (Y0.25Yb0.25Dy0.25Er0.25)B2C2 ceramics. *J. Adv. Ceram.* **2023**, *12*, 1430−1440.

■ NOTE ADDED AFTER ASAP PUBLICATION

This paper was published ASAP on October 20, 2023, with an error in equation 4. The corrected version was reposted October 31, 2023.